RESEARCH PAPER

Passive sorting of emulsion droplets with different interfacial properties using laser-patterned surfaces

Zeeshan Rashid[1] · Ahmet Erten[2] · Berna Morova[3] · Metin Muradoglu[4] · Alexandr Jonáš[5] · Alper Kiraz[1,3]

Abstract
We demonstrate passive sorting of emulsion microdroplets based on differences in their interfacial tension and contact angle. The sorted droplets are flowing inside a microfluidic channel featuring a shallow guiding track (depth $\sim 0.6\,\mu m$) defined by femtosecond laser micromachining in polydimethylsiloxane coating deposited on glass. Under these flow conditions, the droplets experience a confinement force that pulls them into the track; this force depends on the interfacial tension and the difference between the contact angles inside and outside the ablated track. The interplay between the confinement force, fluid drag, and wall friction then determines the trajectory of the droplet along the guiding track. We investigate experimentally the droplet trajectory as a function of droplet velocity and angle between the track and the channel axis and demonstrate precise control of droplet direction by adjusting the track angle. Moreover, we show that droplets of liquids with different interfacial tensions and contact angles travel different distances along the guiding track at a constant flow rate, which can be used for droplet sorting. We develop a theoretical model that incorporates the droplet position with respect to the ablated track, interfacial tension, and contact angles to predict the droplet trajectory under given experimental conditions. Thus, the dynamic behavior of the droplets leading to different guiding scenarios can be studied without the need of computationally expensive fluid dynamics simulations. The presented study paves the way for designing and optimizing new systems for advanced manipulation of droplets of different content using potentially reconfigurable guiding tracks.

✉ Alper Kiraz
akiraz@ku.edu.tr

1   Department of Electrical and Electronics Engineering, Koç University, Sariyer, 34450 Istanbul, Turkey

2   Department of Electronics and Communication Engineering, Istanbul Technical University, Maslak, 34469 Istanbul, Turkey

3   Department of Physics, Koç University, Sariyer, 34450 Istanbul, Turkey

4   Department of Mechanical Engineering, Koç University, Sariyer, 34450 Istanbul, Turkey

5   The Czech Academy of Sciences, Institute of Scientific Instruments, Královopolská 147, 61264 Brno, Czech Republic

1 Introduction

In recent years, droplet-based microfluidics has changed the paradigms for studying chemical and biological processes in research and clinical laboratories, offering the advantages of high throughput, reduced reagent consumption, fast response time and miniaturized spatial requirements. By encapsulating chemical and biochemical reactions in picoliter volume of microdroplets, it has become possible to overcome challenges associated with conventional methods, such as evaporation, complicated fluid handling, dispersion and dilution of reagents, making the analytical and preparative protocols highly efficient and economical (Sims and Allbritton 2007). To date, droplets have been successfully employed as versatile containers carrying chemicals, enzymes, DNA, or even living cells for long-term analysis or further chemical treatment (Yan et al. 2016; Theberge et al. 2010; Bain et al. 2017; Rashid et al. 2018). The advancement in the field of droplet microfluidics requires fast and precise control over the motion of droplet-based reaction containers to direct them to the correct location, for instance, toward the starting position of another experimental protocol or to a

position where they can be analyzed or held for incubation. Sorting of selected droplets moving in a densely populated stream with high sorting speed and accuracy is of paramount importance for high-throughput parallelization of isolated chemical reactions encountered in diagnostic screening or optimization of synthetic protocols (Abate et al. 2010). Such directed manipulation requires a high degree of control over individual droplets with minimal alteration of their chemical composition or physical structure (Ahn and Kerbage 2005).

Droplet manipulation methods can be classified as active or passive. Active manipulation techniques require external mechanisms to control the motion of the droplets, such as light (Fradet et al. 2011; de Saint Vincent et al. 2008; Baret et al. 2009), electric field (Ahn and Kerbage 2005; Guo et al. 2010; Pit et al. 2016), magnetic field (Brouzes et al. 2015), membrane valves (Chen et al. 2016; Abate et al. 2010) or surface acoustic waves (Xi et al. 2017). Since active sorting of droplets typically involves analyzing of the droplet contents, it is quite flexible in terms of selecting the sorting parameter. On the other hand, active sorting protocols require a fast feedback loop that enables actuation of the droplet position or direction of motion on the basis of the outcome of the analysis step, which increases complexity of the microfluidic system. Passive manipulation methods are more straightforward to implement and operate autonomously; however, they require extremely optimized layouts because of the sole dependence on the fluid properties and chip design parameters and do not allow for a wide adjustment of sorting criteria (Rashid et al. 2017). As a consequence, a relatively limited number of works on passive droplet manipulation have been reported in the literature to date. These include viscoelasticity-based sorting in shear gradients (Hatch et al. 2013), size-based sorting using bifurcated channel flow with controlled junction geometry (Tan et al. 2004, 2007), tensiophoresis (Kamalakshakurup and Basu 2013), and hydrodynamic sorting using microfabricated rails (Yoon et al. 2014). None of these prior works have employed differences in interaction energy between the droplets and surfaces with patterned wettability and topography for droplet sorting.

Here, we demonstrate passive sorting of emulsion droplets that is based on the contrast of interfacial tension (IFT) and contact angle (CA) of the droplets with microfabricated guiding tracks obtained by laser ablation of thin polydimethylsiloxane (PDMS) coatings deposited on glass substrates. Schematics of the microfluidic device sections used for droplet generation and sorting are shown in Fig. 1a, b. We show that droplets of pure water dispersed in olive oil are guided more strongly than droplets of water/surfactant mixture due to their larger IFT and higher difference in surface wettability inside and outside the ablated guiding track. We develop a theoretical model of droplet motion including the drag, frictional, and confinement forces (Fig. 1c) acting
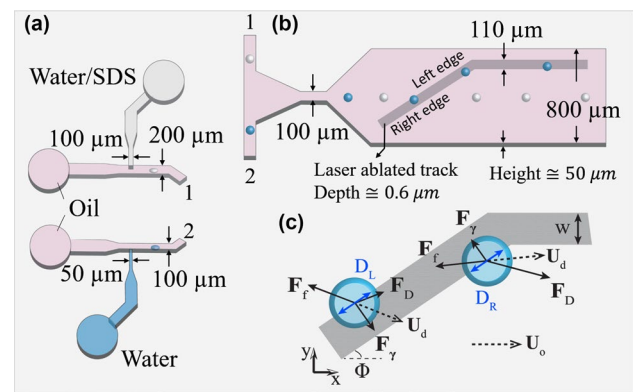

Fig. 1 **a** Top and bottom T-junctions used for droplet generation. **b** Part of the microfluidic chip containing a Hele–Shaw flow channel with a laser-ablated guiding track. **c** Forces acting on a droplet guided along the ablated track. Dark-blue circles indicate the central perimeter of the flattened droplet with radius R_2, light-blue circles concentric with the droplet perimeter indicate the contact area between the droplet and the bottom surface of the flow channel with radius R_B

on a droplet in the Hele–Shaw flow. Droplet trajectory is then obtained neglecting inertial effects, i.e., assuming zero net force acting on the droplet. Subsequently, we match the model results with systematic experiments carried out with water droplets suspended in oil, in which we study the effects of the track slope and droplet flow speed on the stability of droplet guiding. Finally, we demonstrate passive sorting of co-flowing emulsion droplets of water and water/surfactant mixture generated simultaneously in the same chip.

2 Experimental

Microfluidic chips used in the experiments were fabricated from PDMS using standard soft lithography. The chips featured two separate T-junctions for independent generation of droplets of two different liquids, as shown in Fig. 1a. Droplets transported through inlets 1 and 2 merged in a single tapered region with the minimal width of 100 μm (similar to the diameter of flattened droplets) and height of 50 μm that directed the droplets into the center of a Hele–Shaw flow channel (see Fig. 1b). In order to define the droplet guiding tracks, ∼ 0.6-μm-thick PDMS layers were spin-coated on cleaned glass substrates and, subsequently, selectively patterned using femtosecond (fs) laser micromachining. Microfluidic devices were then obtained by aligning and bonding the top PDMS layer containing the 50 μm deep flow channels to the patterned bottom substrate with the droplet guiding track (see details in the ESI). The tracks were designed to have a section inclined at angles Φ of 5° (Chip A), 10° (Chips B, D) and 15° (Chip C) with respect to the axis of the Hele–Shaw channel, followed by a straight section parallel to the channel axis. Chips A, B, and C were used to study

guiding of water droplets at different speeds, whereas Chip D was used to demonstrate sorting of water and water/SDS droplets at a fixed speed of the host liquid flow. For all chips, the width of the track was kept constant at $\sim 110\,\mu m$. Due to slight misalignments of the top and bottom parts of the chip during assembly, the actual values of Φ were measured to be 5.5°, 9.5°, 15.5°, and 10.1° for Chips A, B, C and D, respectively.

For systematic studies of droplet guiding, Chips A, B and C had blocked ports for injecting the dispersed phase into inlet 1. Using independent syringe pumps, olive oil was injected as the continuous phase into both T-junctions and a single dispersed phase (water or water/SDS) was injected into inlet 2. Flow rate of oil into inlet 2 was kept constant at 25 µL/h, while the flow rate of oil into inlet 1 was varied between 20 and 280 µL/h. This scheme worked well for obtaining a broad range of droplet velocities without considerably changing the droplet size. For demonstration of droplet sorting, we used Chip D, in which we generated simultaneously water/SDS and water droplets dispersed in olive oil; these droplets were transported toward the Hele–Shaw channel through inlets 1 and 2, respectively. Water/SDS solutions were prepared with a final SDS concentration of 10 mM and blue dye was added to water droplets in order to distinguish them from co-flowing water/SDS droplets. In the sorting experiments, water and water/SDS were injected at a flow rate of 1 µL/h, while the oil flow rate was kept at 25 µL/h in each inlet. In olive oil, IFT of water/SDS mixture is much smaller than IFT of water ($\gamma_{water/SDS} \sim 2.5$ mN/m (Rashid et al. 2017), $\gamma_{water} \sim 16$ mN/m (Than et al. 1988)). In order to ensure similar sizes of both types of co-flowing droplets, the widths of continuous-phase and dispersed-phase ports in inlet 1, where the water/SDS droplets were produced, were twice as large as the port widths in inlet 2 used for generating the water droplets (see Fig. 1a). The typical lateral diameter $2R_2$ of both types of flattened droplets was about 100 µm.

3 Model for droplet guiding

Our theoretical model of droplet guiding assumes the droplet motion is determined by the interplay between the fluid drag force ($\mathbf{F}_D$), frictional force ($\mathbf{F}_f$) and confinement force ($\mathbf{F}_\gamma$) that are schematically shown in Fig. 1c. Microfluidic devices operate at the low-Reynolds number limit where inertial effects are negligible and the net force acting on the droplet must be 0, i.e., $\mathbf{F}_D + \mathbf{F}_f + \mathbf{F}_\gamma = 0$ at all times. From this force balance, we can determine the instantaneous velocity and position of the droplet flowing within the microfluidic chip. Our droplet guiding experiments were carried out in Hele–Shaw flow geometry, in which the channel height h along the z-axis is much smaller than both the channel width along the y-axis and the channel length along the x-axis. Hence, the scales along the in-plane

directions (x, y) and the out-of-plane direction z separate and the total velocity field $\mathbf{V}(x, y, z)$ of the oil flow can be expressed as $\mathbf{V}(x, y, z) = \mathbf{U}(x, y)f(z)$. Here, $f(z) = (3/2)[1 - (2z/h)^2]$ is a parabolic Poiseuille flow profile and $\mathbf{U}(x, y)$ is the height-averaged in-plane velocity field (Dangla et al. 2011; Beatus et al. 2012). Sufficiently far from the droplet, $\mathbf{U}(x, y)$ becomes equal to the average velocity of oil in the channel, i.e., $\mathbf{U}(x, y) = \mathbf{U}_o$. The value of $\mathbf{U}_o$ corresponding to the actual experiments was determined by dividing the known flow rate of oil by the cross-sectional area of the Hele–Shaw flow channel.

3.1 Forces acting on a droplet

3.1.1 Fluid drag force

Obtained as the sum of pressure drag, $\mathbf{F}_{D,p}$, and viscous drag, $\mathbf{F}_{D,v}$, $\mathbf{F}_D$ is given as (Dangla et al. 2011; Beatus et al. 2012):

$$\mathbf{F}_D = \mathbf{F}_{D,p} + \mathbf{F}_{D,v} = \xi\left(\mathbf{U}_o - \frac{\mathbf{U}_d}{2}\right), \tag{1}$$

where $\xi = 24\pi\mu\frac{R_2^2}{h}\left(1 + 2\frac{K_1(q)}{qK_0(q)}\right)$ is the net drag coefficient, μ is the viscosity of the host fluid, R_2 is the central radius of the droplet flattened between the top and bottom channel walls, h is the channel height, and $\mathbf{U}_o$ and $\mathbf{U}_d$ are the average oil and droplet velocities relative to the channel walls, respectively. Furthermore, $q = 2\sqrt{3}\,R_2/h$ and K_0, K_1 are the modified Bessel functions of the second kind (Pit et al. 2016). In the water/SDS case, the contribution to $\mathbf{F}_D$ due to Marangoni stresses arising from the gradients of IFT is ignored.

3.1.2 Frictional force

Frictional force acting on the moving droplet due to the channel walls is modeled as

$$\mathbf{F}_f = -\beta\mathbf{U}_d, \tag{2}$$

where β is the overall friction coefficient due to viscous dissipation near the rim of the apparent contact line and in the bulk of the droplet liquid and due to repeated pinning and depinning of the droplet contact line from the surface (Beatus et al. 2012; Olin et al. 2013; Butt et al. 2017). The value of β can be determined from experiments with microfluidic chips that do not have ablated guiding tracks (i.e., $\mathbf{F}_\gamma = 0$). At the low-Reynolds number limit that is characteristic for operation of microfluidic devices, inertial effects are negligible and the net force acting on the droplet is zero at all times, i.e., $\mathbf{F}_D + \mathbf{F}_f = 0$. Using the expressions for $\mathbf{F}_D$ and $\mathbf{F}_f$, β is obtained as:

$$\beta = \xi\left(\frac{1}{\alpha} - \frac{1}{2}\right), \tag{3}$$

where $\alpha = |\mathbf{U}_d|/|\mathbf{U}_o|$ is the ratio of terminal speeds of the droplet and the host liquid with respect to the channel walls (Beatus et al. 2012). We note that the value of β for a moving droplet that is crossing the guiding track is expected to be somewhat higher than the value of β measured for the same droplet at the non-patterned section of the fluidic channel. This difference results from the presence of topographic and wettability patterns on the surface, especially near inhomogeneities at the edges of the laser-ablated track. However, such changes of the friction coefficient are difficult to quantify, as this would require the knowledge of the exact profile and texture of the guiding track within the contact area between the droplet and the surface at each point along the droplet trajectory. For this reason, the friction coefficient was only measured in the absence of the track on the channel surface and was assumed to remain approximately constant for guided droplets overlapping with the track.

In our experiments, we determined $\alpha = 0.85$ for water droplets and $\alpha = 1.55$ for water/SDS droplets. Upon inserting these values of α into Eq. (3), we obtain $\beta = 0.68\xi$ for water droplets and $\beta = 0.14\xi$ for water/SDS droplets. Due to the complex nature of friction between the droplets and the channel surface, interpretation of differences in the observed values of β can only be speculative. Our measurements of contact angles reported in the ESI show that water/SDS droplets display consistently higher contact angles on both PDMS and ablated surfaces immersed in olive oil, in comparison with pure water droplets deposited on the same surfaces. Hence, a flattened water/SDS droplet located in the fluidic channel will have a smaller contact area with the channel walls than a water droplet of the same volume, which implies reduced viscous dissipation at the rim of the contact area (Butt et al. 2017). Also, the presence of surfactant in the droplet liquid reduces contact angle hysteresis (Eckmann et al. 2001), which translates into reduced pinning of the droplet contact line on the surface and, thus, smaller resistance of the droplet to translation (Olin et al. 2013). Finally, we can expect that the presence of the surfactant will alter the flow pattern within the droplet; this is associated with changes in the rate of energy dissipation within the droplet and, consequently, changes of the droplet friction coefficient. However, since the dynamics of these phenomena taking place in a moving emulsion droplet interacting with a solid surface of the channel is rather complicated, we did not attempt to quantify them.

3.1.3 Confinement force

While crossing the boundaries of the guiding track, a droplet experiences confinement force, $\mathbf{F}_\gamma$, that is directed perpendicularly to the track boundaries and tends to pull the droplet into the track. In general, $\mathbf{F}_\gamma$ arises from changes of the droplet shape (Dangla et al. 2011) and CA (Pit et al. 2016)

upon entering or leaving the track. Confinement force $\mathbf{F}_{\gamma,s}$ acting on a droplet with IFT γ due to a change of its surface area A is equal to the negative gradient of the surface energy $E = \gamma A$ of the droplet: $\mathbf{F}_{\gamma,s} = -\nabla E = -\gamma \nabla A$. When the droplet crosses the edge of the guiding track, its surface area changes only when the droplet has a displacement component in the direction ζ perpendicular to the track edge; thus, $F_{\gamma,s} = -\gamma \, dA/d\zeta$. In our calculations, we approximate the actual value of $F_{\gamma,s}$ that depends on ζ by its average value estimated from the total change in the droplet surface area ΔA (Fradet et al. 2011):

$$F_{\gamma,s} = -\gamma \frac{dA}{d\zeta} \approx -\gamma \frac{\Delta A}{\Delta \zeta} = -\gamma \frac{\Delta A}{2R_B} . \tag{4}$$

In Eq. (4), $\Delta A = (A_{in} - A_{out})$ $[\Delta A = (A_{out} - A_{in})]$ is the change of the total droplet surface area upon moving completely from the outside to the inside [from the inside to the outside] of the track [detailed expressions for A_{in} and A_{out} are given in the ESI]. The corresponding droplet displacement perpendicular to the track edge is then $\Delta \zeta = 2R_B$, equal to the diameter of the droplet contact area with the bottom channel surface (see Fig. 1c). We assume R_B does not change when the droplet is inside and outside the track. Variations in surface wettability inside and outside the ablated guiding track lead to an additional component of the confinement force, $F_{\gamma,w}$, that is proportional to γ and to the difference of cosines of CAs θ_{in} and θ_{out} inside and outside the track (Pit et al. 2016). Moreover, $F_{\gamma,w}$ also depends on the length of the boundaries between the regions of the droplet-channel contact area that are located inside and outside the track. Combination of $F_{\gamma,s}$ and $F_{\gamma,w}$ then gives the total confinement force F_γ as:

$$F_\gamma = F_{\gamma,s} + F_{\gamma,w} = -\gamma \frac{\Delta A}{2R_B} + \gamma \left(D_L - D_R\right)\left(\cos \theta_{in} - \cos \theta_{out}\right),$$
$$\tag{5}$$

where D_L and D_R are the lengths of chords defined by the overlap of the circular contact area of radius R_B between the droplet and the channel surface with the left and right track edge, respectively (see Fig. 1c).

θ_{out} and θ_{in} were measured by direct imaging of $10\,\mu L$ droplets deposited on surfaces immersed in olive oil to be $\theta_{out} = 172°(177°)$ and $\theta_{in} = 167.5°(172°)$ for water (water/SDS) droplets (see Sect. 3 in the ESI). We note that our model of droplet guiding is only an approximation, as it replaces the actual spatially dependent force $F_{\gamma,s}$ with its constant averaged value, does not explicitly include the presence of a thin lubricating film of the host liquid between the droplet and the channel surface and neglects the effects of roughness and chemical heterogeneity of the ablated track surface that cause pinning of the contact line and contact angle hysteresis (Quere 2008). However, despite these limitations, the model is still capable of capturing

semi-quantitatively the essential trends observed in the droplet guiding experiments with different emulsion systems under a wide range of experimental conditions. In our experiments, surface roughness (Smith et al. 2012), van der Waals interactions (Khodaparast et al. 2017), and curvature of the channel walls (Muradoglu and Stone 2007) may be contributing toward rupturing of the lubricating films inside the guiding tracks, and hence, enabling sorting based on the interfacial properties of the droplets.

3.2 Finite difference time approach for modeling of droplet motion

By equating the net force acting on the droplet to zero, i.e., $\mathbf{F}_D + \mathbf{F}_f + \mathbf{F}_\gamma = 0$, the following expressions are obtained for the x and y components of $\mathbf{U}_d$:

$$U_{d,x} = \frac{\xi U_o + F_\gamma \sin \Phi}{\beta + \xi/2} \tag{6a}$$

$$U_{d,y} = -\frac{F_\gamma \cos \Phi}{\beta + \xi/2}, \tag{6b}$$

where Φ denotes the track angle (see Fig. 1c). In deriving Eqs. (6a) and (6b), we assumed the oil velocity $\mathbf{U}_o$ is directed along the x-axis, even though $\mathbf{U}_o$ must also have a component along the y-axis in the tapered transition zone at the beginning of the Hele–Shaw cell, since the flow streamlines have to expand to cover the full width of the channel. However, this transverse component of $\mathbf{U}_o$ is too small to cause any observable deflection of the droplet trajectory from the x-axis before the droplet encounters the guiding track, as confirmed by the experimental videos provided in the ESI. Moreover, the droplets enter the Hele–Shaw cell along its axis, where the transverse component of $\mathbf{U}_o$ must be zero due to the symmetry. Thus, we neglected the y-component of $\mathbf{U}_o$ in the calculations. In our simulations, the droplet position and velocity are first initialized to zero, and then Eqs. (6a) and (6b) are used to update the values of $U_{d,x}$ and $U_{d,y}$. To this end, in the ith simulation step, D_R and D_L are calculated from the actual droplet position (x_i, y_i) and the corresponding value of F_γ is then calculated using Eq. (5). After updating the droplet velocity [$(U_{d,x})_i, (U_{d,y})_i$], the position of the droplet in the $(i + 1)^{th}$ time step is calculated as $x_{i+1} = x_i + (U_{d,x})_i \Delta t$, $y_{i+1} = y_i + (U_{d,y})_i \Delta t$. This multi-step iterative approach enabled us to determine the position and velocity of the droplet at each time step.

Starting from the initial position, simulated droplet trajectories first cross the left edge of the track, remain within the track for a certain amount of time, and finally leave the track by crossing its right edge. While the contact area between the droplet and the channel surface is either completely outside or completely inside the guiding track, the

confinement force $F_\gamma = 0$. Upon intersecting of the contact area with either of the track edges, F_γ starts acting on the droplet in the direction perpendicular to the track edges and pointing into the track. In particular, at the left track edge, F_γ points downwards and to the right, which, as a convention, is assumed to be the positive direction. Similarly, when the droplet intersects with the right track edge, F_γ points upwards and to the left, i.e., in the negative direction (see Fig. 1c). Figure 2 shows the calculated magnitudes of both $F_{\gamma,s}$ and $F_{\gamma,w}$ for a water droplet with the lateral diameter $2R_2 = 100$ µm moving across the guiding track in Chips A, B and C. As soon as the contact area between the droplet and the bottom channel surface crosses the left edge of the track, $F_{\gamma,s}$ and $F_{\gamma,w}$ become non-zero and start deflecting the droplet trajectory from its original direction along the x-axis. A similar deflection then takes place at the right edge of the track. As the droplet traverses the edges of the track, $F_{\gamma,s}$ (green curves) given by Eq. (4) remains constant, whereas $F_{\gamma,w}$ (blue curves) evolves with the droplet position according to Eq. (5). The analysis presented in Fig. 2 illustrates that, for our geometrical parameters (channel height, track depth), magnitudes of both $F_{\gamma,s}$ and $F_{\gamma,w}$ are comparable. Hence, we always consider both of these confinement forces in our calculations.

4 Results and discussion

Figure 3a–c show experimental and theoretical trajectories of water droplets in Chips A, B, and C, respectively. The experimental trajectories of flowing droplets sampled at the frame rate of 19 fps were determined by video analysis using a normalized cross-correlation algorithm that also revealed droplet velocities at different positions along the trajectory (Rashid et al. 2017). In each sub-figure, the left plot shows experimental and theoretical trajectories for 5 exemplary droplets moving at different speeds (movies available in the ESI), while the right plot shows all experimental trajectories recorded in the given chip for more than 30 droplets moving at different speeds. At low U_d, water droplets are observed to be fully guided. As U_d increases, the droplets start following the guiding track only partially, leaving the track at a particular distance ΔH (the track exit height) measured along the y-axis with respect to the center of the Hele–Shaw channel. Specifically, a droplet is considered fully guided if $\Delta H > \Delta H_{thr}$, where ΔH_{thr} is the threshold value measured from the center of the Hele–Shaw channel to the lower edge of the horizontal section of the track, as shown in Fig. 3b. ΔH_{thr} for Chips A, B and C was measured to be 260 µm, 270 µm and 270 µm, respectively. Differences in ΔH_{thr} observed for each chip are due to slight misalignment of the droplet guiding tracks with the Hele–Shaw channels during the chip assembly. After leaving the guiding track, some
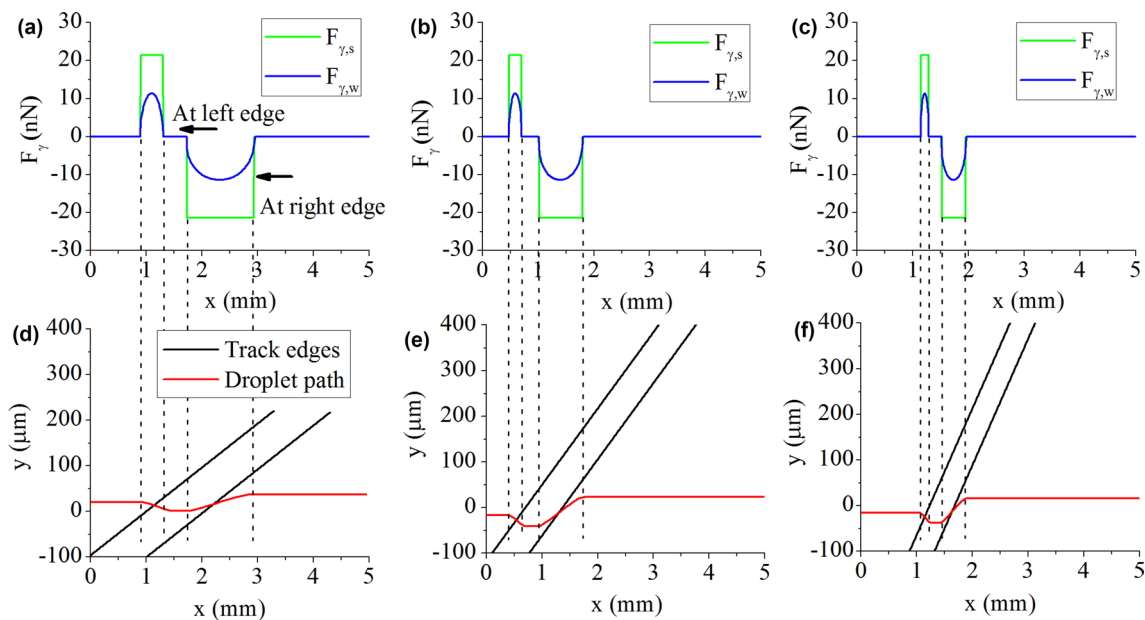
Fig. 2 Calculated profiles of confinement forces $F_{\gamma,s}$ (green curves) and $F_{\gamma,w}$ (blue curves) acting on a water droplet with the lateral diameter $2R_2 = 100$ μm crossing the track edges in **a** Chip A ($U_d = 2357$ μm/s), **b** Chip B ($U_d = 985$ μm/s) and **c** Chip C ($U_d = 528$ μm/s). Corresponding trajectories for the same droplet and flow conditions in **d** Chip A, **e** Chip B and **f** Chip C. In all plots, horizontal axis indicates the position of the droplet center along the channel axis
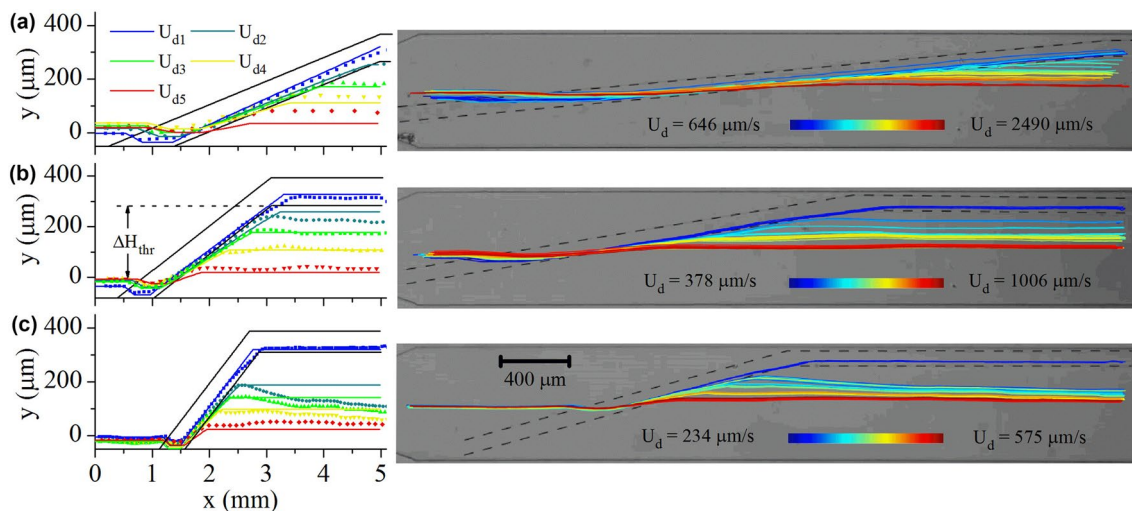
Fig. 3 (left) Experimental (dotted) and theoretical (solid) trajectories of water droplets flowing at different U_d in **a** Chip A [$U_{d(1,2,3,4,5)} = (660, 1060, 1218, 1533, 2357)$ μm/s], **b** Chip B [$U_{d(1,2,3,4,5)} = (378, 463, 490, 510, 985)$ μm/s] and **c** Chip C [$U_{d(1,2,3,4,5)} = (234, 272, 293, 347, 528)$ μm/s]. Black lines represent the track edges. (right) Experimental trajectories of all water droplets studied in the given chip. Coloring of droplet trajectories indicates the values of U_d according to the respective color maps

droplets located in the central region of Chip C are observed to move slightly downwards, at an angle with respect to the channel axis. This behavior was not observed during the initial experiments performed with the same chip (see ESI for details) and it is most likely caused by contamination of

the chip surface that creates an additional confinement barrier for the droplets.

Figure 4a shows the variations of ΔH as a function of U_d and capillary number $\text{Ca} = \mu U_d/\gamma$ measured for water droplets in Chips A, B and C, together with the theoretical predictions. Values of $\Delta H > \Delta H_{thr}$ reached at low U_d indicate
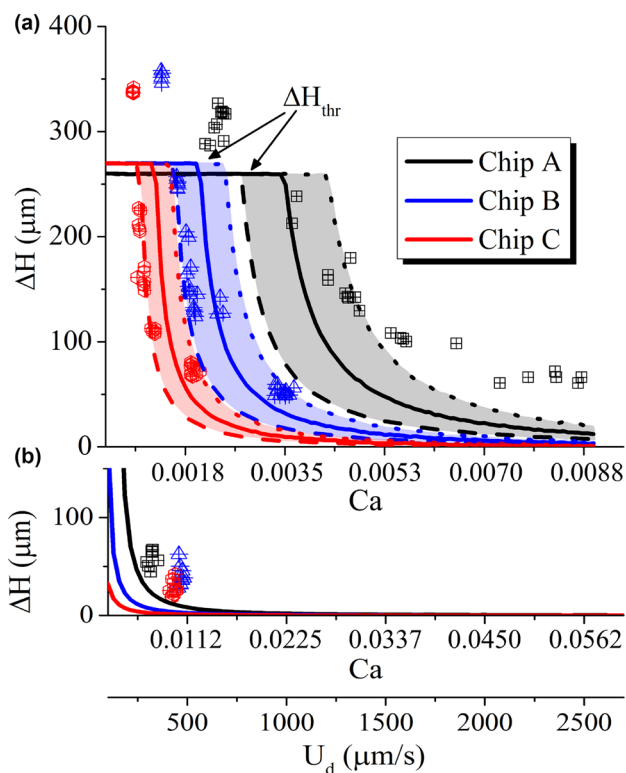
Fig. 4 Track exit height ΔH of **a** water and **b** water/SDS droplets as a function of U_d and Ca. For each chip shown in part **a**, the three smooth curves indicate theoretical results obtained with track depth of 0.4 μm (– –), 0.6 μm (—), and 0.8 μm (...). In part **b**, track depth is assumed to be 0.6 μm. U_d axis is the same in both **a** and **b**

full droplet guiding. The theoretical plots were obtained assuming three different depths of the guiding track: 0.4 μm (– –), 0.6 μm (—) and 0.8 μm (...). Recorded surface profiles revealed average track depths of ∼ 0.6 μm measured between the track center and the level of the surface far away from the ablated track. However, the laser ablation process leaves residual PDMS accumulated near the track edges, which causes uncertainties in the actual track depth. A good match is observed between the experiments and theoretical results, especially for Chips B and C. For $U_d > 1000$ μm/s, the droplets in all three chips are observed to undergo a

slight vertical deflection, contrasting with the prediction $\Delta H \to 0$ for increasing U_d. We attribute this disagreement to the presence of inhomogeneities at the track edge that further enhance the droplet confinement within the track. In addition, the model does not include the full details of droplet deformation upon its interaction with the track. In accordance with the expectations, Fig. 4a shows that—for similar values of U_d—guiding of water droplets is improved, (i.e., larger values of ΔH are reached) with decreasing Φ. This dependence of ΔH on U_d can be also used for directing droplets with different speeds to specific streamlines located at different positions along the *y*-axis in the microfluidic device. Results of guiding experiments performed in Chips *A*, *B*, and *C* with water/SDS droplets are summarized in Fig. 4b, together with the theoretical predictions. For this case, both experiments and theory indicate very small partial guiding of the droplets. Similarly to the case of pure water droplets, experiments show stronger guiding than predicted by theory. This residual guiding can be mainly attributed to inhomogeneities present at the track edges and additional deformations of the droplet upon entering the track that are not included in the model, which assumes a perfect rotational symmetry of the droplets. However, even for the water/SDS droplets, the values of Ca used in the experiments are smaller than 0.012 (see Fig. 4b). Thus, any distortions of the droplet shape due to shear forces induced by the flow of the host liquid are expected to be small (Stone 1994). Figure 4a, b show a clear contrast in the values of ΔH observed for water and water/SDS droplets for the same chip configuration and U_d. This large contrast constitutes the essence of the droplet sorting mechanism demonstrated in this paper.

Sorting of water and water/SDS droplets of similar sizes that are concurrently generated in Chip *D* is demonstrated in Fig. 5. In these experiments, T-junctions in inlets 1 and 2 were used for generating water/SDS and water droplets, respectively, and the rate of droplet generation from both T-junctions was sufficiently low to ensure the propagation of individual droplets in the Hele–Shaw channel without merging. Figure 5a shows two experimental trajectories observed for exemplary water and water/SDS droplets (dotted lines) together with theoretical trajectories (solid lines). These
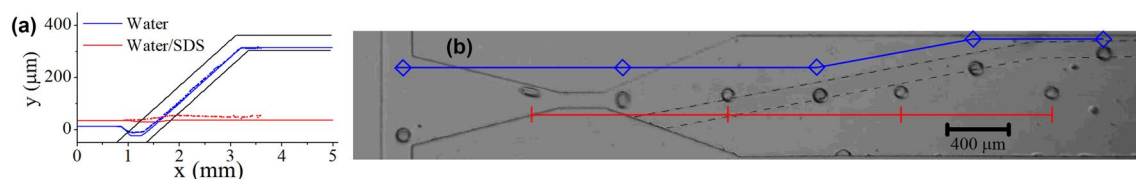

Fig. 5 Sorting of water ($U_d = 337$ μm/s) and water/SDS ($U_d = 609$ μm/s) droplets co-flowing in Chip *D*. **a** Experimental (dotted) and theoretical (solid) trajectories of water and water/SDS droplets. Black lines represent the track edges. **b** Merged image showing the trajectories followed by a water (blue symbols) and water/SDS (red symbols) droplet in Chip *D*. Water/SDS droplet can be identified by its slightly lighter color and increased deformation due to higher speed and lower IFT

trajectories clearly indicate that the water droplet is fully guided, while the water/SDS droplet is virtually unaffected by the track presence. Figure 5b presents an exemplary image demonstrating sorting of water and water/SDS droplets. This image was obtained by merging camera frames recorded at different times (see movie S16 in the ESI), and it shows consecutive positions of the same water and water/SDS droplet while moving within the microfluidic chip.

5 Conclusions

We have introduced a method for passive sorting of droplets in microfluidic chips on the basis of their different interfacial properties. To this end, we have used surfaces with topographic and wettability patterns represented by inclined guiding tracks prepared by laser micromachining. We have developed a theoretical model of droplet guiding that predicts the droplet trajectory from the balance of fluid drag, frictional and confinement forces acting on the droplet and have found a good agreement between the model and experiments performed with water and water/SDS droplets at different flow speeds and track inclination angles. We have also demonstrated sorting of water and water/SDS droplets of similar sizes that are simultaneously generated by two different T-junctions in the same microfluidic chip. The presented approach can be used to design custom microfluidic devices for guiding and passive sorting of droplets without extensive fine tuning of experimental protocols. This approach can also be used to characterize interaction between droplets and surfaces of materials with wettability tunable by external mechanisms such as electric field (Mannetje et al. 2014) or light (Lim et al. 2006).

References

Abate AR, Agresti JJ, Weitz DA (2010) Microfluidic sorting with high-speed single-layer membrane valves. Appl Phys Lett 96:203509

Ahn K, Kerbage C (2005) Dielectrophoretic manipulation of drops for high-speed microfluidic sorting devices. Appl Phys Lett 88:24104

Bain RM, Sathyamoorthi S, Zare RN (2017) On-droplet chemistry: the cycloaddition of diethyl azodicarboxylate and quadricyclane. Angew Chem Int Edn 56:15083–15087

Baret JC, Miller OJ, Taly V, Ryckelynck M, Harrak AE, Frenz L, Rick C, Samuels ML, Hutchison JB, Agresti JJ, Link DR, Weitz DA, Griffiths AD (2009) Fluorescence-activated droplet sorting: efficient microfluidic cell sorting based on enzymatic activity. Lab Chip 9:1850–1858

Beatus T, Bar-Ziv RH, Tlusty T (2012) The physics of 2D microfluidic droplet ensembles. Phys Rep 516:103–145

Brouzes E, Kruse T, Kimmerling R, Strey HH (2015) Rapid and continuous magnetic separation in droplet microfluidic devices. Lab Chip 15:908–919

Butt H-J, Gao N, Papadopoulos P, Steffen W, Kappl M, Berger R (2017) Energy dissipation of moving drops on superhydrophobic and superoleophobic surfaces. Langmuir 33:107–116

Chen Y, Tian Y, Xu Z, Wang X, Yu S, Dong L (2016) Microfluidic droplet sorting using integrated bilayer micro-valves. Appl Phys Lett 109:143510

Dangla R, Lee S, Baroud CN (2011) Trapping microfluidic drops in wells of surface energy. Phys Rev Lett 107:12450

de Saint Vincent MR, Wunenburger R, Delville JP (2008) Laser switching and sorting for high speed digital microfluidics. Appl Phys Lett 92:154105

Eckmann D, Cavanagh D, Branger A (2001) Wetting characteristics of aqueous surfactant-laden drops. J Colloid Interface Sci 242:386–394

Fradet E, McDougall C, Abbyad P, Dangla R, McGloin D, Baroud CN (2011) Combining rails and anchors with laser forcing for selective manipulation within 2D droplet arrays. Lab Chip 11:4228–4234

Guo F, Ji XH, Kan Liu RXH, Zhao LB, Guo ZX, Liu W, Guo SS, Zhao XZ (2010) Droplet electric separator microfluidic device for cell sorting. Appl Phys Lett 96:193701

Hatch AC, Patel A, Beer NR, Lee AP (2013) Passive droplet sorting using viscoelastic flow focusing. Lab Chip 13:1308–1315

Kamalakshakurup G, Basu AS (2013) Size based droplet sorting with wide tuning range using tensiophoresis

Khodaparast S, Atasi O, Deblais A, Scheid B, Stone HA (2017) Dewetting of thin liquid films surrounding air bubbles in microchannels. Langmuir 34:71–99

Lim HS, Han JT, Kwak D, Jin M, Cho K (2006) Photoreversibly switchable superhydrophobic surface with erasable and rewritable pattern. J Am Chem Soc 128:14458–14459

Mannetje D, Ghosh S, Lagraauw R, Otten S, Pit A, Berendsen C, Zeegers J, van den Ende D, Mugele F (2014) Trapping of drops by wetting defects. Nature Comm 5:1–7

Muradoglu M, Stone HA (2007) Motion of large bubbles in curved channels. J Fluid Mech 570:455–466

Olin P, Lindstrom SB, Pettersson T, Wagberg L (2013) Water drop friction on superhydrophobic surfaces. Langmuir 29:9079–9089

Pit AM, Bonestroo S, Wijnperle D, Duits MHG, Mugele F (2016) Electrode-assisted trapping and release of droplets on hydrophilic patches in a hydrophobic microchannel. Microfluid Nanofluid 20:1–12

Quere D (2008) Wetting and roughness. Annu Rev Mater Res 38:71–99

Rashid Z, Morova B, Yaman O, Soydan S, Birer O, Yilgor I, Kiraz A (2018) Reconfigurable and permanent wetting patterns on polymer surfaces obtained using plasma oxidation and laser ablation. Opt Data Process Storage 4:22–29

Rashid Z, Coskun UC, Morova Y, Morova B, Bozkurt AA, Erten A, Jonas A, Akturk S, Kiraz A (2017) Guiding of emulsion droplets in microfluidic chips along shallow tracks defined by laser ablation. Microfluid Nanofluid 21

Sims CE, Allbritton NL (2007) Analysis of single mammalian cells on-chip. Lab Chip 7:423–440

Smith JD, Dhiman R, Anand S, Reza-Garduno E, Cohen RE, McKinley GH, Varanasi KK (2012) Droplet mobility on lubricant-impregnated surfaces. Soft Matter 9:1772–1780

Stone H (1994) Dynamics of drop deformation and breakup in viscous fluids. Annu Rev Fluid Mech 26:65–102

Tan YC, Fisher JS, Lee AI, Cristini V, Lee AP (2004) Design of microfluidic channel geometries for the control of droplet volume, chemical concentration, and sorting. Lab Chip 4:292–298

Tan YC, Ho YL, Lee AP (2007) Microfluidic sorting of droplets by size. Microfluid Nanofluid 4:343–348

Than P, Preziosi L, Josephl D, Arney M (1988) Measurement of interfacial tension between immiscible liquids with the spinning road tensiometer. J Colloid Interface Sci 124:552–559

Theberge AB, Courtois F, Schaerli Y, Fischlechner M, Abell C, Hollfelder F, Huck WTS (2010) Microdroplets in microfluidics: an evolving platform for discoveries in chemistry and biology. Angew Chem Int Edn 49:5846–5868

Xi HD, Zheng H, Guo W, Calvo AMG, Ai Y, Tsao CW, Zhou J, Li W, Huang Y, Nguyen N-T, Tan SH (2017) Active droplet sorting in microfluidics: a review. Lab Chip 17:751–771

Yan X, Bain R, Cooks RG (2016) Organic reactions in microdroplets: reaction acceleration revealed by mass spectrometry. Angew Chem Int Edn 55:12960–12972

Yoon DH, Numakunai S, Nakahara A, Sekiguchi T, Shoji S (2014) Hydrodynamic on-rail droplet pass filter for fully passive sorting of droplet-phase samples. RSC Adv 4:37721–37725